IMMUNOLOGY

Microscale combinatorial stimulation of human myeloid cells reveals inflammatory priming by viral ligands

Miguel Reyes[1,2]*†, Samantha M. Leff[1,2], Matteo Gentili[1], Nir Hacohen[1,3]*, Paul C. Blainey[1,2,4]*

Cells sense a wide variety of signals and respond by adopting complex transcriptional states. Most single-cell profiling is carried out today at cellular baseline, blind to cells' potential spectrum of functional responses. Exploring the space of cellular responses experimentally requires access to a large combinatorial perturbation space. Single-cell genomics coupled with multiplexing techniques provide a useful tool for characterizing cell states across several experimental conditions. However, current multiplexing strategies require programmatic handling of many samples in macroscale arrayed formats, precluding their application in large-scale combinatorial analysis. Here, we introduce StimDrop, a method that combines antibody-based cell barcoding with parallel droplet processing to automatically formulate cell population × stimulus combinations in a microfluidic device. We applied StimDrop to profile the effects of 512 sequential stimulation conditions on human dendritic cells. Our results demonstrate that priming with viral ligands potentiates hyperinflammatory responses to a second stimulus, and show transcriptional signatures consistent with this phenomenon in myeloid cells of patients with severe COVID-19.

INTRODUCTION

Single-cell RNA sequencing (scRNA-seq) has been widely adopted as a profiling tool in biology and translational medicine, with studies routinely analyzing thousands of cells (1). Most studies thus far have focused on cataloging cells in different tissues across health and disease (2–4), followed by clustering or matrix decomposition to identify cell states and gene programs. While useful in identifying disease-associated states and functional programs, data from observational studies seldom provide mechanistic insight into which specific factors are required to induce the observed responses. Bottom-up approaches, wherein cells at baseline are exposed to various environmental triggers to recapitulate disease-associated states, provide a way to address this question. However, finding the appropriate combination of factors for a given cell state is a difficult challenge as cells are exposed to complex milieus in vivo.

Innate immune cells, such as macrophages and dendritic cells, are evolved to sense a wide variety of pathogenic and endogenous signals (5, 6). They respond by coordinating an inflammatory or an antiviral response, which are primarily driven by the nuclear factor κB (NFκB) and interferon regulatory factor (IRF) pathways, respectively (7). These transcriptional programs are often up-regulated in human diseases (8–12), but the specific combination of factors that induce these changes is difficult to determine. Individual ligands are sensed by different receptors but may converge toward the same downstream signaling pathway, and any combination of ligands may contribute to the overall response (13). A number of studies (14–16) have also shown that sequential exposure of myeloid cells to different combinations of pathogen-related ligands can result in history-dependent functional responses.

Profiling the response of myeloid cells to combinations of immune stimuli can provide clues about how disease-associated myeloid states are induced and improve our understanding of host responses in diseases with complex triggers (17, 18). However, a systematic analysis of combinations of primary and secondary stimulations (hereinafter referred to as "prime" and "challenge" treatments, respectively) has not been performed because of the experimental complexity and the large quantities of cells and reagents required to test a wide array of ligand combinations (19–22). To address this problem, we developed a technology that enables systematic combinatorial testing of mammalian cell culture conditions using droplet microfluidics. We previously developed a drug discovery platform that allows for high-throughput construction of pairwise combinations for bacterial growth assays (23). Here, we developed a new workflow on this platform to perform multiplexed stimulation of mammalian cells in droplets and recover the cells for molecular profiling ("StimDrop"; Fig. 1A). StimDrop enables automated assembly and labeling of cells in pairwise conditions with parsimonious utilization of samples and reagents, and exploits the high cellular throughput of scRNA-seq to read out responses across a wide array of conditions. Using StimDrop, we demonstrate that human myeloid cells primed with viral ligands have sustained expression of antiviral genes over several days, which increases their inflammatory response to secondary challenge.

RESULTS

Development and validation of StimDrop

To perform StimDrop, immune cell populations or stimuli are first emulsified with oligonucleotide-conjugated antibodies (24) to encode the identities of different cell populations and challenge stimuli, respectively. Droplets are then pooled and loaded in a microwell array where pairs assemble spontaneously en masse in an arrayed format. Adjacent droplets are subsequently merged, and

[1]Broad Institute of MIT and Harvard, Cambridge, MA, USA. [2]Department of Biological Engineering, Massachusetts Institute of Technology, Cambridge, MA, USA. [3]Center for Cancer Research, Massachusetts General Hospital and Harvard Medical School, Boston, MA, USA. [4]Koch Institute for Integrative Cancer Research at MIT, Cambridge, MA, USA.
*Corresponding author. Email: msreyes@broadinstitute.org (M.R.); nhacohen@broadinstitute.org (N.H.); pblainey@broadinstitute.org (P.C.B.)
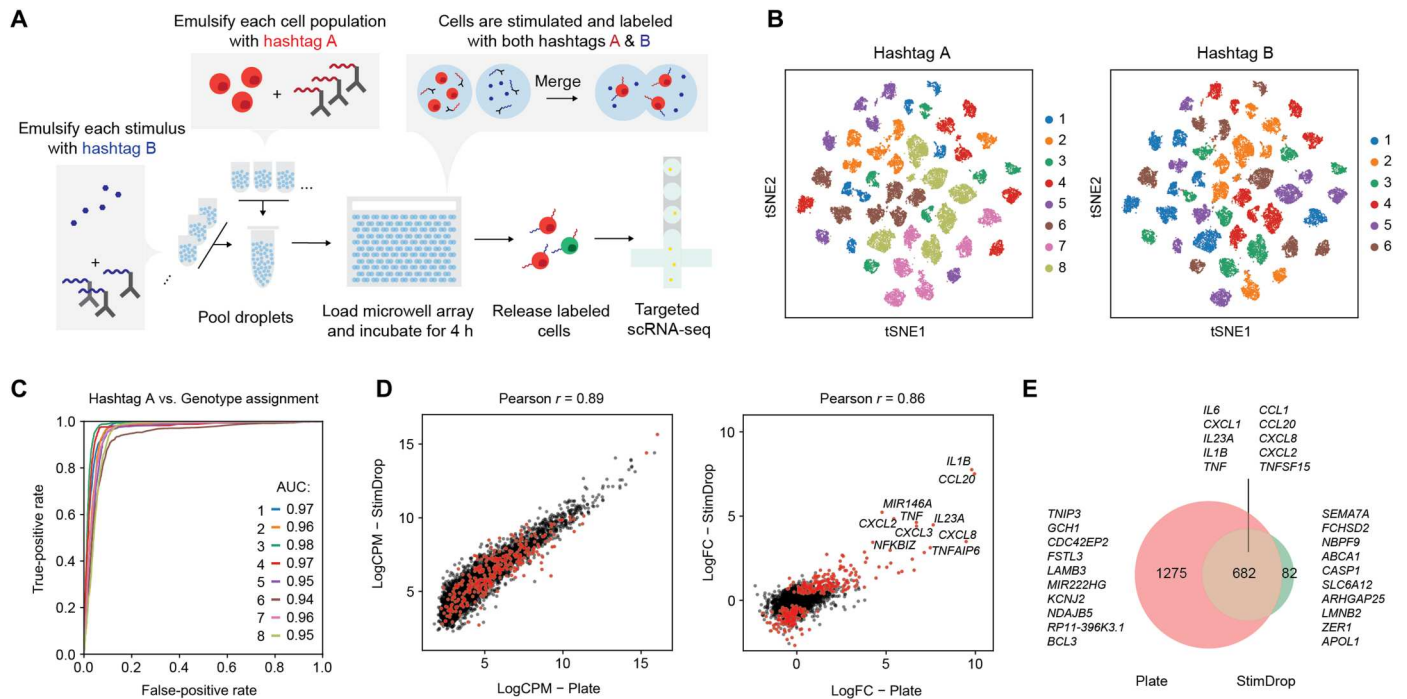†Present address: Department of Infectious Diseases, Genentech, South San Francisco, CA, USA.

Fig. 1. StimDrop enables systematic combinatorial analysis of mammalian cell culture conditions. (**A**) Schematic of the StimDrop workflow. (**B**) Hashtag-based tSNE projection of cells from a pilot 8 × 6 StimDrop experiment. tSNE coordinates are calculated on the basis of normalized, log-transformed hashtag counts, and cells are labeled on the basis of donor hashtag (A, left) and stimulus hashtag (B, right) assignments. (**C**) Receiver operating characteristic (ROC) curves for cell assignment–based hashtag counts from StimDrop. Cell assignments based on genotypes were treated as the true label for each cell. (**D**) Scatterplots showing the logCPM (counts per million, left) or $\log_2$FC (fold change, right) of each gene after treatment of MDDCs with Pam3CSK4 in a 96-well plate (x axis) or through StimDrop (y axis). Genes with false discovery rate (FDR) < 0.01 are highlighted in red, and the top 10 genes with the highest fold-change values are shown. n = 4 replicates were performed for each condition. (**E**) Venn diagram showing overlap of differentially expressed genes (FDR < 0.01, edgeR exact test) between Pam3CSK4-treated MDDCs in a plate or through StimDrop. Top 10 genes with the highest fold changes in the intersection or set differences are indicated.

the chip is incubated to simultaneously stimulate and additionally barcode the cell populations according to challenge stimuli exposure. The cells are then released from the chip and profiled using a commercial high-throughput scRNA-seq platform. The barcodes are sequenced alongside mRNAs using a previously established library construction protocol (*24*), and dual barcodes are used to identify the sample from which each cell originated and the challenge stimulus each received in the microfluidic chip. In initial experiments, we noted no significant change in cell viability for peripheral blood mononuclear cells (PBMCs) from healthy donors after droplet merging and incubation over time (fig. S1A). Furthermore, we were able to modulate the number of cells that are encapsulated in each 1-nL droplet from less than 1 to more than 10 by changing the initial concentration of cells that are emulsified to adjust cellular throughput and desired influence of paracrine signaling among cells (fig. S1B). The data presented here were collected from emulsions containing an average of about five cells per droplet.

To determine the feasibility of our barcoding approach, we first tested in-droplet antibody labeling using fluorophore-conjugated antibodies. We emulsified PBMCs, fluorescein isothiocyanate (FITC)–CD45, and phycoerythrin (PE)–CD45 antibodies separately and pooled the emulsions in a 2:1:1 ratio before loading the microwell array. Upon incubation, we observed labeling of the cells in droplets after 30 min, as evidenced by the emergence of puncta with high PE and FITC signals in pairs of droplets that contain both cells and the corresponding fluorescent antibody (fig. S1C). To

quantitatively assess the fraction of cells that are labeled, we released the cells from the microwell device and measured cellular fluorescence via flow cytometry (fig. S1D). The fractions of unlabeled, PE-positive, and FITC-positive cells are approximately 2:1:1, as expected from random pairwise assembly of our initial droplet populations. A small fraction of cells (7.5%) are labeled with both PE and FITC antibodies, which could be attributed to loading of wells with >2 droplets, or limited cross-labeling of the cells during the release protocol. Next, we performed a pilot combinatorial labeling experiment by emulsifying PBMCs from eight individual donors with unique donor-specific hashtag antibodies (hashtag A). In addition, we emulsified six unique hashtag B antibodies separately as stimulus droplets. Both PBMC and stimulus droplets were pooled and loaded in the microwell array, and the chip was incubated for 4 hours at 37°C before releasing the cells for scRNA-seq. T-distributed stochastic neighbor embedding (tSNE) of the cells based on hashtag counts showed 48 distinct clusters corresponding to each PBMC donor and stimulus pair (Fig. 1B). Sample assignments from the hashtag counts show high concordance with genotype-based identification (area under the receiver operating characteristic > 0.94; Fig. 1C), demonstrating the accuracy of our barcoding strategy.

Next, we assessed the effect of the StimDrop workflow on the functional response of human myeloid cells. We used human monocyte-derived dendritic cells (MDDCs) as a model system due to their compatibility with suspension culture. We used bulk

RNA-seq to profile the transcriptional response of MDDCs to a Toll-like receptor (TLR) ligand, Pam3CSK4, using StimDrop and a conventional plate-based assay. Both expression levels and fold change of genes upon stimulation of MDDCs correlated strongly between StimDrop and the standard plate-based assay (Pearson $r = 0.89$ and 0.86, respectively; Fig. 1D). Several key inflammatory genes that have the highest fold changes were both detected in the plate-based assay and StimDrop, although more genes were significantly up-regulated in the plate-based assay, perhaps due to technical effects of the StimDrop workflow on MDDCs (Fig. 1E and fig. S2A). To address this question, we systematically assessed the response of MDDCs in various incubation conditions related to StimDrop. We found that incubation of MDDCs with hashtag antibodies or fluorocarbon oil does not substantially alter their transcriptional response, but emulsification of the cell suspension does (fig. S2B). Emulsification and incubation of MDDCs in nanoliter droplets result in up-regulation of inflammation-associated genes, including the tumor necrosis factor α (TNFα) and NFκB signaling pathways, perhaps due to the induction of a stress response in MDDCs (fig. S2, C and D). This response, however, was substantially weaker (fourfold) when compared with the response of MDDCs to TLR stimulation with Pam3CSK4 (fig. S2, E and F). These results demonstrate that StimDrop retains ample dynamic range to effectively capture the response of MDDCs to TLR stimulation despite some effects of encapsulation and droplet incubation on their transcriptional profile.

Analysis of prime and challenge combinations with StimDrop

To perform a combinatorial serial stimulation experiment on MDDCs with StimDrop, we first generated custom hashtag antibodies to secure the 72 (64 × 8) barcodes needed for this experiment (Materials and Methods and fig. S3). Next, we profiled the response of CD14+ monocytes to immune stimuli spanning the diverse classes of innate immune receptors (TLRs, nucleotide oligomerization domain-like receptors, DNA sensors, RNA sensors, C-type lectin receptors, and inflammasomes). From the resulting profiles, we derived a set of prestimulation ligands and appropriate concentration ranges (Materials and Methods, fig. S4, and table S1).

We performed an initial StimDrop experiment examining the effect of 64 priming conditions (21 unique immune ligands with three concentrations and one untreated control) on the response of MDDCs to eight subsequent challenge ligands introduced 5 days after priming (Fig. 2A). Using a targeted panel of immune-related genes, we measured the transcriptional profiles of MDDCs 4 hours after challenge, sampling a median of 15 cells for each prime × challenge pair (Materials and Methods and fig. S5). By applying consensus nonnegative matrix factorization (cNMF) (25) on the resulting data, we found multiple gene programs expressed by MDDCs. Of these programs, two correspond to inflammatory and antiviral responses of myeloid cells, which strongly vary in response to stimulus (Fig. 2, B and C, and fig. S6, A and B). In the absence of priming, MDDCs showed increased usage of the inflammatory module upon incubation with the seven challenge ligands we tested (Fig. 2D).

We found that cells primed with nucleic acid/viral ligands [transfected double-stranded RNA, poly(I:C), poly(dA:dT), and hpRNA] have increased expression of the antiviral program after challenge, even with challenges that otherwise activate the

inflammatory program (Fig. 2, D and E). This effect is observed across all challenge conditions, and the magnitude is dependent on both the dose and identity of the priming ligand (Fig. 2F). To validate this finding, we performed a StimDrop experiment on two independent donors with a limited set of priming conditions (fig. S7, A to C). We found a similar set of gene programs corresponding to inflammatory and antiviral responses, although two distinct antiviral programs were detected by cNMF in the validation experiment (fig. S7, D and E). Similar to our initial results, we found that priming with poly(I:C) and poly(dA:dT) resulted in a dose-dependent increase in expression of antiviral programs in monocytes independent of challenge (fig. S7, F and G). These results suggest that stimulation of monocytes with viral ligands results in sustained expression of antiviral genes, which can last for at least 6 days independent of later challenges with other ligands.

Sustained expression of antiviral genes and chromatin remodeling in primed cells

To validate the priming effect we observed in our StimDrop experiments, we profiled the transcriptional response of poly(dA:dT)- and phosphate-buffered saline (PBS)–primed cells over time (Fig. 3, A and B). We found that treatment of monocytes with poly(dA:dT) results in a strong acute transcriptional response, as evidenced by the large number of differentially expressed genes between primed and unprimed cells at 8 hours (fig. S8A). Priming with poly(dA:dT) increases both inflammatory and antiviral gene programs initially; however, the antiviral program remains up-regulated for several days after priming (Fig. 3C). After 6 days, several interferon (IFN)–related genes are still differentially expressed between primed and unprimed cells (fig. S8B). These results support the findings from our initial StimDrop experiment that treatment with a viral ligand results in sustained expression of an antiviral gene program.

We hypothesized that the durable up-regulation of the antiviral gene program could be attributed to chromatin remodeling. Poly(dA:dT)-primed cells show marked differences in accessible chromatin when compared with nontreated controls (Fig. 3D). Analysis of open chromatin peaks shows increased accessibility of genomic loci with IRF and signal transducer and activator of transcription (STAT) motifs (Fig. 3E) and increased promoter accessibility of antiviral genes, which also correlates with increased expression (Fig. 3F). Of note, *TNF*, a gene that is common to the inflammatory and antiviral gene programs detected in the StimDrop experiment, shows a peak with a marked increase in accessibility near its promoter region, although neither the IRF nor STAT motif is detectable within this peak (Fig. 3G).

We also examined other phenotypic effects of poly(dA:dT) by measuring cell numbers, viability, activation of caspase-1, and levels of surface markers in MDDCs after priming. We found no substantial difference in cell numbers or viability between primed and unprimed cells (fig. S8, C and D) but noted an increase in the fraction of cells with active caspase-1 4 days after priming (fig. S8E). This result is expected because poly(dA:dT) has been shown to activate the AIM2 inflammasome in myeloid cells (26). In addition, priming with poly(dA:dT) does not result in substantial changes in TLR4 or CD14 expression after 6 days of culture (fig. S8, F and G). We did observe a reduction in the expression of CD209, a marker specific to MDDC differentiation with granulocyte-macrophage colony-stimulating factor (GM-CSF) and interleukin-4 (IL-
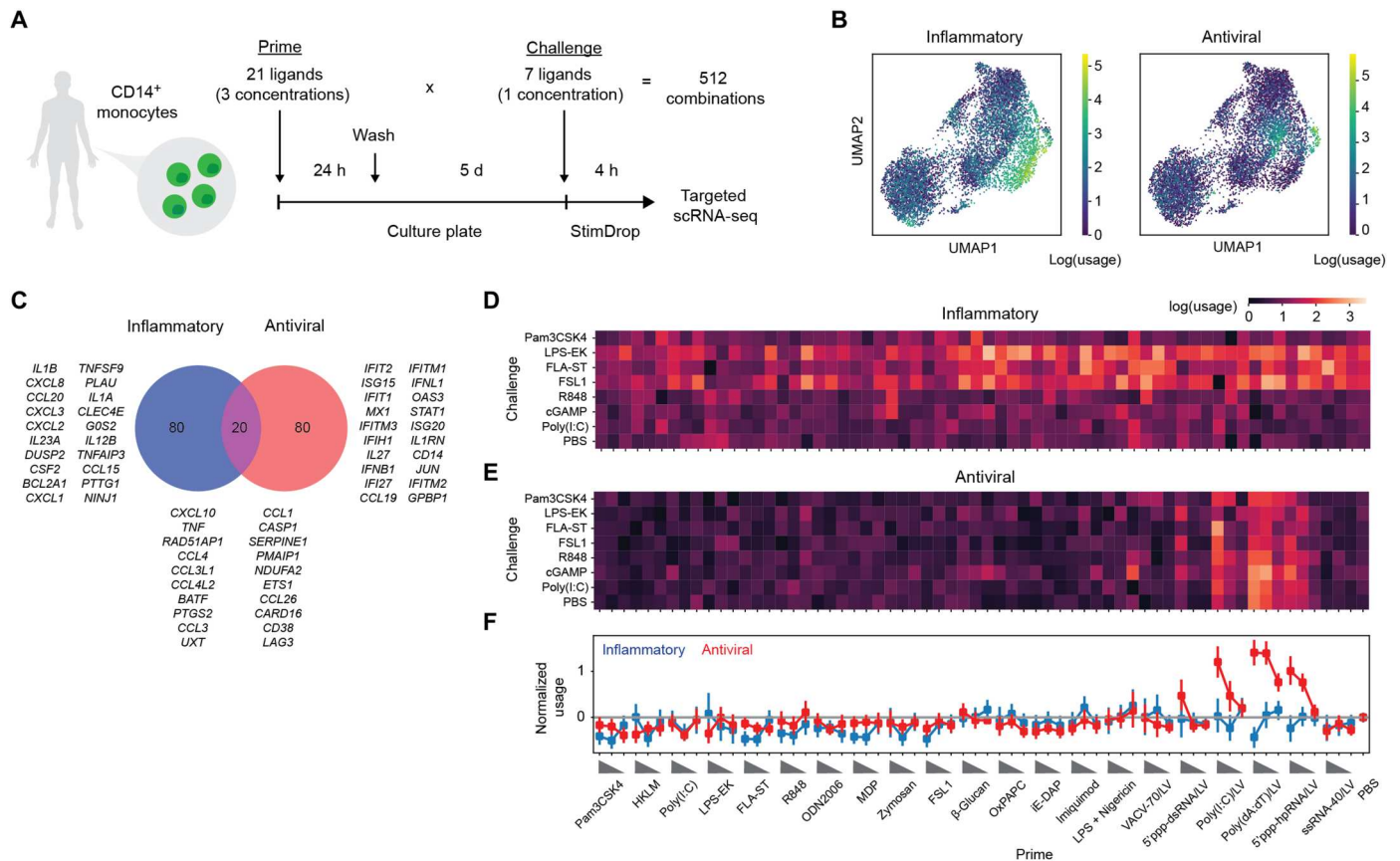
Fig. 2. Analysis of prime and challenge combinations using StimDrop identifies stable antiviral responses. (**A**) Schematic of the StimDrop experiment analyzing prime × challenge combinations in human MDDCs. (**B**) Uniform manifold approximation (UMAP) embedding of dendritic cells from the primary StimDrop experiment (*n* = 8570 cells). Cells are colored by usage of the inflammatory (left) and antiviral (right) gene programs. (**C**) Venn diagram of the top 100 genes with the highest loadings in each program (left, inflammatory; right, antiviral). (**D** and **E**) Heatmap showing the mean usage value of the inflammatory (D) and antiviral (E) gene program for each pair of prime and challenge conditions. (**F**) Relative usage of the inflammatory (blue) and antiviral (red) gene programs for each priming condition in the primary Stim-Drop experiment. Usage values are averaged across all challenge conditions and normalized to the PBS priming condition. Error bars indicate the 95% confidence interval of the mean.

4) (*27*, *28*). Analysis of published transcriptional data of human dendritic cells (*29*) also shows that signatures of priming are enriched in the DC4 cluster (fig. S8H). These results suggest that priming may have an effect on the polarization and differentiation of MDDCs, in addition to inducing sustained antiviral gene expression.

Increased inflammatory responses to secondary challenge in primed cells

We examined the functional effect of viral ligand priming on MDDCs after secondary challenge by staining for intracellular TNFα, IL-1β, and ISG15 after challenge (Fig. 4, A and B). As expected from our transcriptional findings, a high fraction of cells are positive for ISG15 after priming with poly(I:C) or poly(dA:dT), independent of challenge (Fig. 4B). Unexpectedly, we found that priming with poly(dA:dT) substantially increases the fraction of TNFα- and IL-1β–positive cells after challenge with TLR ligands, and a similar but weaker effect is also observed in poly(I:C)-primed cells after lipopolysaccharide (LPS) and R848 challenge (Fig. 4B). The increase in fraction of TNFα+ cells is only detectable 5 days after priming with poly(dA:dT), suggesting a delayed effect of

priming on increasing inflammatory responses (fig. S8I). In addition, we saw that the degree of increase in TNFα expression is proportional to the increase in ISG15 expression across donors and priming conditions, demonstrating a link between the degree of antiviral program induction and the subsequent increase in inflammatory responses (Fig. 4C). Priming with recombinant IFNβ, but not IFNγ, also results in an increase in the fraction TNFα+ cells after LPS challenge, suggesting that the priming effect may be due to activation of the IRF pathway (fig. S8J). We performed similar experiments in both monocyte-derived macrophages and MDDCs primed with varying concentrations of poly(dA:dT) and found a dose-dependent increase in the fraction of TNFα+ cells for all challenge conditions (Fig. 4D). Although we did not find significant increases in the expression of *TNF* and *IL1B* transcripts in primed cells in our StimDrop experiment, these results show that priming with viral ligands enhances inflammatory responses to subsequent TLR challenge at the protein level.

Transcriptional responses in our StimDrop experiments were read out with a targeted panel of immune genes, limiting our capacity to find potential mechanisms behind increased inflammatory responses in primed cells. To characterize the transcriptional
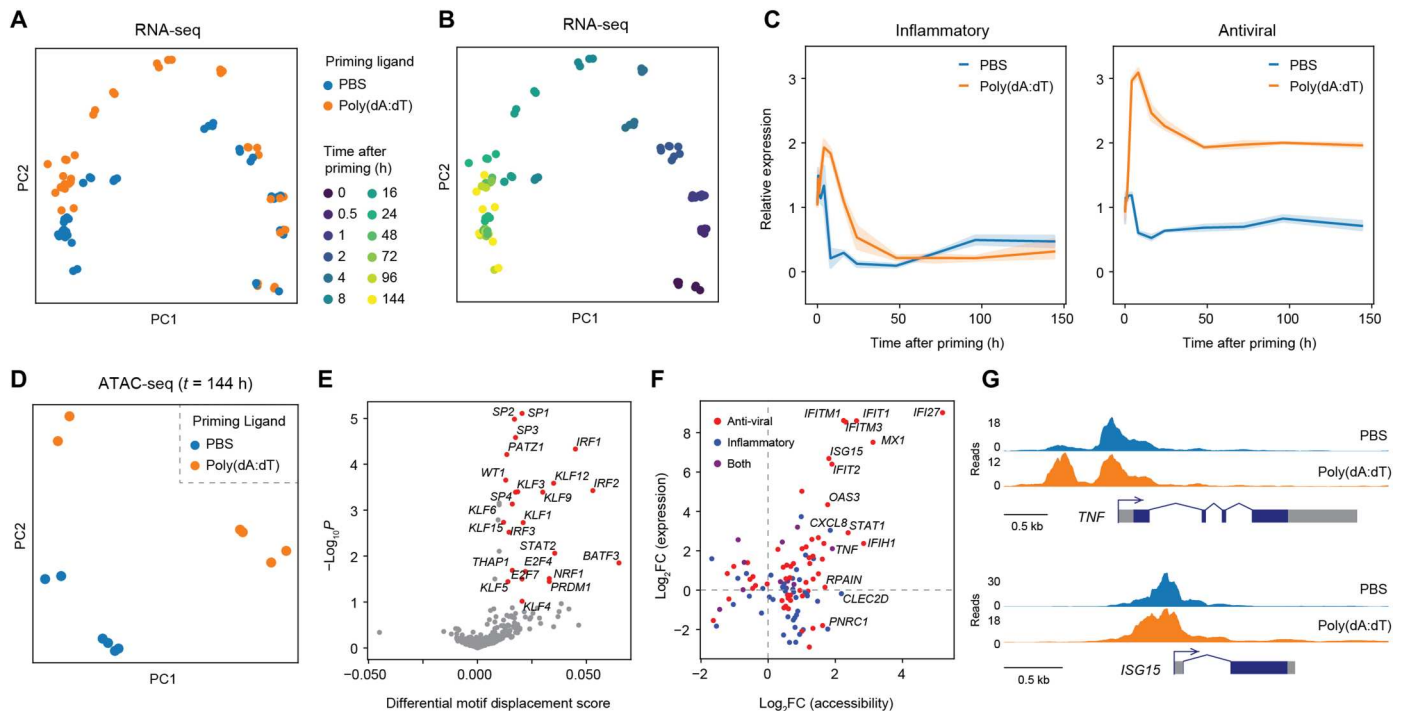
Fig. 3. Sustained expression of antiviral genes and chromatin remodeling in viral ligand–primed MDDCs. (A and **B**) Principal components analysis (PCA) plots of the transcriptional profiles measured by bulk RNA-seq of PBS and poly(dA:dT)-primed MDDCs. Points are colored by prestimulation (A) or time point (B). RNA-seq experiments were performed on two donors with two technical replicates each. (**C**) Relative expression of the inflammatory (left) and antiviral programs (right) in primed (orange) or unprimed (blue) MDDCs over time. Expression scores are calculated by taking the average expression of the top 50 genes for each module, subtracted with the average expression of a randomly sampled reference set of 50 genes. (**D**) PCA plot of the chromatin accessibility profiles measured by ATAC-seq of PBS and poly(dA:dT)-primed MDDCs on day 6. ATAC-seq experiments were performed on three donors with two technical replicates each. (**E**) Volcano plot showing differential motif accessibility between poly(dA:dT)- and PBS-primed cells. Transcription factors with significantly enriched motifs are indicated in red ($P < 0.1$). (**F**) Differential promoter accessibility (x axis) and expression (y axis) of the top 100 genes of the inflammatory and antiviral gene programs. (**G**) Genome tracks of the ATAC-seq data for *TNF* and *ISG15*.

signatures of sequential stimulation more deeply, we performed whole-transcriptome scRNA-seq on MDDCs with or without priming and challenge (fig. S9). Similar to our StimDrop experimental results, we found no substantial difference in the usage of the inflammatory gene program or expression of *TNF* and *IL1B* in primed versus unprimed cells after challenge with LPS (fig. S9, C to E). However, by performing differential expression analysis between PBS- and LPS-challenged cells for each priming condition, we found differences in the number of genes that are up- or down-regulated and the regulatory effect magnitudes (Fig. 4E). A number of IFN-associated genes, for example, are up-regulated in unprimed cells but are down-regulated in poly(dA:dT)-primed cells, and a higher number of genes are differentially expressed in unprimed cells compared with primed cells (Fig. 4F). These differences could perhaps be attributed to the already increased expression of antiviral genes in poly(dA:dT)-primed cells even in the absence of challenge. In addition to these differences, we found a limited number of genes that are uniquely up-regulated in poly(dA:dT)-primed cells after LPS challenge (Fig. 4F). Among these are *KDM6B* and *DOT1L*, which have both been previously shown to modulate proinflammatory responses in macrophages (*30–32*). This analysis suggests that up-regulation of a unique set of genes could result in enhanced production of TNFα- and IL-1β proteins even without further increases in *TNF* and *IL1B* transcript

expression. Furthermore, up-regulation of these genes in myeloid cells may indicate the response of primed cells to challenge.

Analysis of viral priming signatures in severe COVID-19

Severe acute respiratory syndrome coronavirus 2 (SARS-CoV-2) infection activates antiviral gene programs in myeloid cells (*33, 34*), and severe cases of coronavirus disease 2019 (COVID-19) are typically associated with hyperinflammation (*35*). Among patients with SARS-CoV-2 infection, those with severe disease have higher levels of circulating inflammatory cytokines (*36–38*) and increased expression of inflammatory genes in airway myeloid cells (*39–42*). A number of studies (*43–45*) have proposed that severe cases of SARS-CoV-2 infection might result from coinfection with bacterial pathogens, as evidenced by the increased levels of endotoxin and bacterial DNA observed in patients' blood. Given these findings, we hypothesized that transcriptional signatures of viral priming and subsequent challenge can be detected in myeloid cells from patients with COVID-19.

To test this hypothesis, we performed a meta-analysis of three scRNA-seq datasets (*39, 40, 46*) with cells from bronchoalveolar lavage (BAL) fluid of patients with COVID-19 (Fig. 5A). We performed cNMF on myeloid cells from each dataset and found four common gene modules, including the inflammatory and antiviral programs, in all three datasets (Fig. 5B and fig. S10). We found that usage of the antiviral gene program is similar between mild
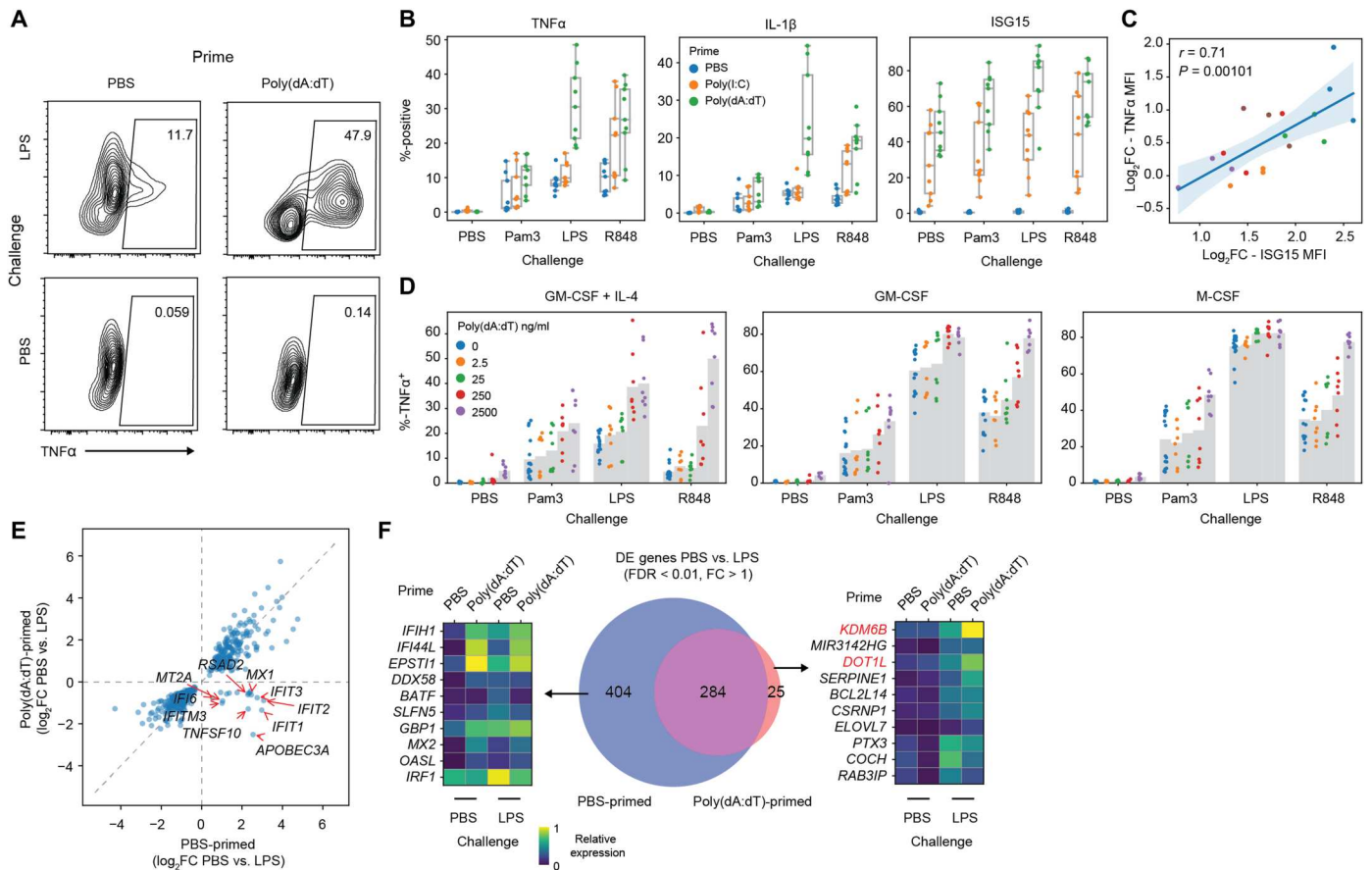
Fig. 4. Increased inflammatory response of primed MDDCs to secondary challenge. (**A**) Representative plots of TNFα intracellular cytokine staining of PBS and poly(dA:dT)-primed MDDCs with or without LPS challenge. (**B**) Fraction of TNFα (left), IL-1β (middle), and ISG15 (right) among cells from the indicated prime [transfected poly(dA:dT) or poly(I:C) (1 μg/ml)] and challenge conditions [LPS (100 ng/ml), Pam3CSK4 (1 μg/ml), or R848 (1 μg/ml)] measured by intracellular cytokine staining. Experiments were performed in three donors with three replicates for each condition. Boxes show the median and interquartile range (IQR) for each condition, with whiskers extending to 1.5 IQR in either direction from the top or bottom quartile. (**C**) Scatterplot showing the fold change in ISG15 mean fluorescence intensity (MFI; x axis) and TNFα (y axis) across donors. Line and shadow indicate linear regression fit and 95% confidence interval, respectively. Significance of the correlation (Pearson r) was calculated with a two-sided permutation test. (**D**) Fraction of TNFα-positive cells after challenge with the indicated stimuli. Colors indicate the concentration of poly(dA:dT) used for priming. Experiments were performed on three donors with three replicates each. (**E**) Scatterplot shows the fold change (FC) for each gene after challenge with LPS of PBS-primed (x axis) or poly(dA:dT)-primed MDDCs. Top 10 genes with the highest fold change in the bottom right quadrant are labeled. (**F**) Venn diagram (middle) showing overlap of differentially expressed genes (FDR < 0.01, Wilcoxon rank sum test) between PBS-primed (x axis) and poly(dA:dT)-primed MDDCs after LPS challenge. The top 10 genes with the highest fold changes in the set differences are indicated, and their average expression across the different prime and challenge conditions is shown in the heatmaps (left and right).

and severe cases of COVID-19 but is substantially higher when comparing COVID-19 with healthy controls and non–COVID-19 pneumonia (Fig. 5C). Usage of the inflammatory gene program, on the other hand, is significantly higher in severe versus mild COVID-19. Of note, expression of both *KDM6B* and *DOT1L* in myeloid cells is also higher in severe COVID-19 when compared with mild cases and healthy controls (Fig. 5D). A similar increase is observed in comparing COVID-19 versus non–COVID-19 pneumonia for *DOT1L* but not *KDM6B*. Expression of *DOT1L* is also positively correlated with increased usage of the inflammatory gene program across all datasets (Fig. 5E). On the basis of our previous findings, the concomitant increases in inflammatory program usage and *DOT1L* expression in severe COVID-19 could signify the response of viral ligand–primed myeloid cells to a secondary challenge.

To further explore these signatures in a large cohort of COVID patients, we analyzed the expression of the antiviral and inflammatory programs and *DOT1L* in bulk RNA-seq profiles of BAL cells from 299 patients (*39*). As expected, among patients with pneumonia, antiviral program usage is higher in COVID-19 patients, while inflammatory program usage is similar (Fig. 5F). Of note, COVID-19 patients later in their disease course (>7 days from intubation) have higher *DOT1L* expression than patients with non–SARS-CoV-2 pneumonia. In addition, among patients with COVID-19, those with superinfections (bacterial and/or fungal infection in addition to SARS-CoV-2; 24 of 68 patients) have increased usage of the inflammatory gene program (Fig. 5G). These patterns are likely driven by myeloid cells given that the majority of cells in BAL from scRNA-seq data in the same study are macrophages (61.7 ± 14.5%). These associations are consistent with the model
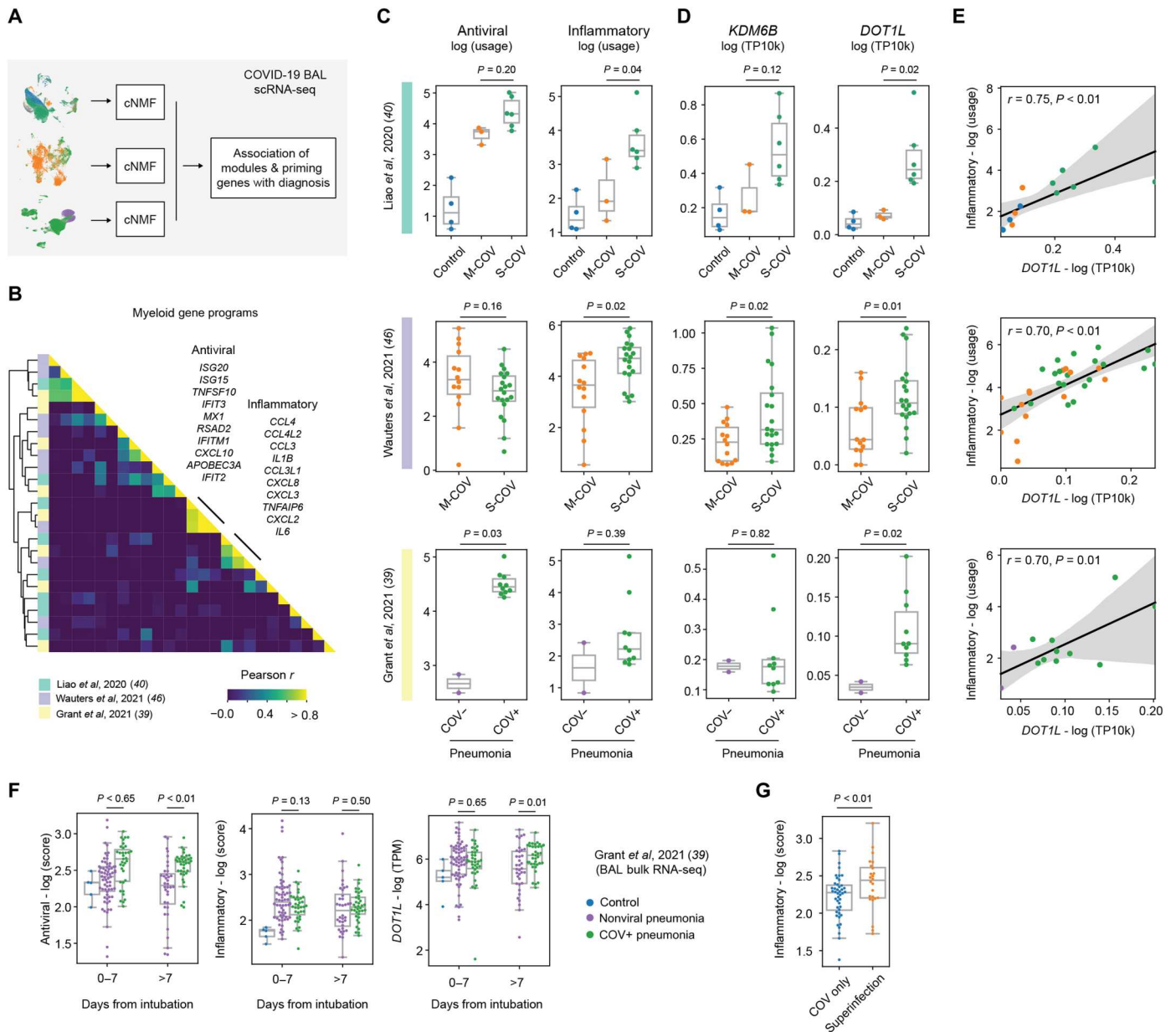
Fig. 5. Signatures of sequential viral priming and secondary challenge in severe COVID-19. (**A**) Analysis scheme for three BAL scRNA-seq datasets from cohorts of COVID-19 patients. (**B**) Correlation matrix of the gene loadings (*z* scores) for the myeloid gene expression programs across the three BAL scRNA-seq datasets. Gene expression modules were derived in an unbiased manner from each dataset using cNMF. The common modules corresponding to the inflammatory and antiviral programs, and the top 10 genes with the highest loadings in each, are indicated. (**C**) Mean usage (log) of the antiviral (left) and inflammatory (right) gene expression programs in myeloid cells from each patient across patient groups for each dataset. (**D**) Mean expression of *KDM6B* (left) and *DOT1L* (right) in myeloid cells from each patient across patient groups for each dataset. (**E**) Scatterplot showing mean *DOT1L* expression (*x* axis) and inflammatory module usage (*y* axis) across patients in each dataset. Line and shadow indicate linear regression fit and 95% confidence interval, respectively, and significance of the correlations (Pearson *r*) was calculated with a two-sided permutation test. (**F**) Mean program score of the antiviral (left) and inflammatory (middle) gene expression programs and mean *DOT1L* expression (right) in BAL transcriptional profiles for each patient across the indicated cohorts and time points. (**G**) Mean program score of the inflammatory gene expression program in patients with COVID-19 only or superinfection. For all boxplots (C, D, F, and G), boxes show the median and IQR for each patient cohort, with whiskers extending to 1.5 IQR in either direction from the top or bottom quartile. Significance values (*P*) were calculated with a Wilcoxon rank sum test. M-COV, mild COVID-19; S-COV, severe COVID-19.

that secondary stimulation (from either bacterial ligands or endogenous damage–associated proteins) following the initial viral infection contributes to inflammation associated with severe COVID-19.

DISCUSSION

Our findings highlight the need for systematic analysis of cellular responses to complex stimuli and the inadequacy of baseline molecular profiling to explain important cellular responses in disease. Technologies enabling facile large-scale stimulation experiments like StimDrop are needed to advance our understanding of immunological phenomena, such as the effect of sequential stimulation on myeloid cells. Through StimDrop, we found that priming with viral ligands induces sustained expression of antiviral genes in MDDCs and macrophages, increasing their inflammatory response to secondary challenge. We also show that among patients with COVID-19, signatures of sequential priming and challenge can be detected in patients with severe illness.

Bacterial coinfection has long been known to play a key role in severe cases of viral disease such as influenza (17). Previous studies in vivo have demonstrated that coinfection or sequential infection with viruses and bacteria result in hyperinflammatory responses (47, 48). Our results align with these findings and further suggest a long-term effect of antiviral priming on the induction of hyperinflammatory responses. Our StimDrop and in vitro experiments with human cells demonstrate that this phenotype is still detectable multiple days after the initial stimulation. Given these findings, we hypothesize that sustained activation of an antiviral response followed by an inflammatory response to additional pathogen or damage-associated ligands may contribute to exacerbated inflammatory pathology in severe COVID-19. This is supported by a recent study suggesting that gut microbiome dysbiosis and translocation are associated with disease severity in patients with SARS-CoV-2 (49). Additional analysis of samples from patients are needed to determine whether similar signatures can be detected in other viral infections, including influenza. Further studies are also needed to dissect the mechanism through which viral ligands prime myeloid cells in this system and to determine whether modulating related pathways can reduce the inflammatory burden of viral disease.

Our study demonstrates the utility of parallel droplet assembly in exploring a large space of experimental conditions with mammalian cells. This platform can be further extended to higher-order combinations, which we have previously demonstrated for microbial culture (50). In addition, parsimonious use of cells in emulsions could allow the application of multiplexed stimulations to limited samples from primary tissues or clinical specimens and experiments exploring large combinatorial stimulation spaces. Arrayed control of both cell identity and density in droplets could further enable the study of cell-cell interactions. At present, the StimDrop workflow can be readily applied to various suspension cell types and stimulation conditions, but further development is needed to enable manipulation of adherent cells. Our technical validation experiments also indicate that the droplet encapsulation of dendritic cells induces a detectable stress response. Cell encapsulation conditions, such as cell density, droplet encapsulation pressure, or medium/surfactant composition, may be further optimized to ameliorate this effect, especially in sensitive and difficult to culture cell types (51). In light of the increasing throughput of scRNA-seq and

continued development of cellular labeling strategies (52–55), our technology is poised to become a useful tool for pairing combinatorial perturbation experiments with single-cell transcriptional readouts and for identifying sets of factors that induce disease-associated transcriptional states.

MATERIALS AND METHODS

Blood monocyte isolation, differentiation, and stimulation

PBMCs were isolated from leukocyte reduction collars obtained from healthy donors. Leukocyte reduction collars were obtained from discarded clinical samples through the Crimson Core at the Brigham and Women's Hospital (Boston, MA) with anonymized donor information (https://crimson-core.partners.org/). Research on the samples was approved by Institutional Review Boards at the Broad Institute of MIT and Harvard and Brigham and Women's Hospital. Concentrated blood containing leukocytes was diluted 1:1 with 1× PBS, layered on top of Ficoll-Paque Plus (GE Healthcare), and centrifuged at 1200g for 20 min at 20°C. The PBMC layer was retrieved, resuspended in RPMI 1640 (Gibco), and centrifuged again at 400g for 8 min. CD14+ monocytes were enriched with the CD14 Microbeads (Miltenyi Biotec). Isolated CD14+ cells were validated using flow cytometry (CD14-FITC, clone M5E2, BioLegend) to be of >90% purity.

Monocytes were cultured in RPMI 1640 supplemented with 10% heat-inactivated fetal bovine serum (FBS; Gibco) at 37°C. For dendritic cell differentiation, 50 ng/mL GM-CSF and IL-4 (PeproTech) were added to the medium. For macrophage differentiation, 50 ng/mL GM-CSF or M-CSF (PeproTech) was added. Cytokines were replenished every 2 to 3 days of culture.

For sequential stimulation experiments, cells were incubated with the indicated priming ligand for 16 hours immediately after isolation. The cells were then washed with PBS, resuspended in fresh medium, and cultured for another 5 days without pathogen ligand stimulation. On day 6, the cells were restimulated with the indicated challenge ligand. Cells were challenged for 4 and 6 hours for RNA-seq and intracellular cytokine staining experiments, respectively.

Microfluidic device fabrication

The microfluidic device was fabricated using a previously published protocol (23). Briefly, 100- to 120-μm features (array of two circles with a diameter of 150 μm, set at 10% overlap; spaced 50 μm apart) were patterned on silicon wafer molds by ultraviolet exposure (OAI 206 Mask Aligner) of SU8-2050 photoresist (Microchem). Chips were fabricated by soft lithography from polydimethylsiloxane (PDMS; Dow Corning Sylgard) and coated with 1.5-μm parylene C (Paratronix).

StimDrop: Chip operation and cell extraction

Device setup was performed using a previously published protocol (23) with minor modifications. To minimize technical artifacts from the workflow, steps involving the handling of live cells were performed at 4°C. Briefly, 20 μl of each input (either cell suspensions or stimuli) was pipetted into a Bio-Rad QX200 cartridge, using fluorocarbon oil [3M Novec 7500 + 0.5% (w/w) RAN Biotech 008-FluoroSurfactant] as the continuous phase. The Bio-Rad QX200 instrument was used to emulsify inputs into 1-nl droplets. Cells were emulsified at 5 M/ml cell suspensions to achieve an

average of five cells per droplet. After emulsifying all cell and stimulus suspensions, cell and stimulus droplets were each pooled separately and then combined to achieve a 1:1 ratio of cells to stimuli.

To prepare for loading, the PDMS chip was mounted on a custom-designed acrylic loader such that the chip was suspended ~500 μm above a glass slide. The PDMS chip was then washed by pipetting 5 ml of fluorocarbon oil without surfactant into the flow space between the chip and glass slide. After draining the oil from the acrylic loader, 200 μl of the pooled emulsion was injected into the flow space. The loader was tilted to move the emulsion through the flow space and allow the aqueous droplets to load onto the microwells. After loading, the chip was washed 3× with 5 ml of fluorocarbon oil without surfactant to remove excess droplets. The chip was then carefully removed from the acrylic loader and sealed using a Microseal B film (Bio-Rad). To merge the pairs of droplets in each microwell, a sheet of laboratory tissue wiper (Kimtech) was gently pressed onto the surface of the Microseal B film. The chip was inspected using a stereomicroscope to ensure that >95% of droplet pairs have been merged. The chip was transferred (seal-side down) to a 10-cm culture dish and submerged in PBS. The dish was then transferred to a 37°C 5% CO_2 incubator for 4 to 6 hours.

After incubation, the chip was removed from the dish and wiped to remove any excess PBS. The film seal was then gently removed from the surface of the chip. To extract the cells from the chip, 5 ml of cold medium (RPMI 1640 supplemented with 10% FBS, Gibco) was pipetted over the chip to dislodge the cell-containing droplets from the microwells. The runoff containing the cells was collected in a 25-ml reservoir. This process was repeated until >90% of the wells have been emptied (confirmed by inspection under a stereomicroscope). The medium containing cells was then transferred to a 15-ml tube and spun down at $100g$ for 1 min to pellet any residual oil. The aqueous layer was then collected and spun down at $300g$ for 5 min, and the cell pellet was resuspended at 1000 cells/μl in cold medium for scRNA-seq.

Flow cytometry and intracellular cytokine staining
The following fluorescent antibodies were used in this study: CD45-PE (clone 2D1), CD45-FITC (clone 2D1), CD14-FITC (clone M5E2), CD209-PE (clone DCS-8C1), CD86-PE (clone IT2.2), CD169-APC (allophycocyanin) (clone 7-239), and CD284-PE (clone HTA125). After staining, cells were resuspended in fluorescence-activated cell sorting (FACS) buffer with 2% CountBright beads (Invitrogen) and 4′,6-diamidino-2-phenylindole (DAPI) (0.1 μg/ml) to allow determination of absolute counts and live cells during analysis. Intracellular staining was performed using a Cytofix/Cytoperm kit (BD Biosciences), following the manufacturer's protocol. Cells were stained with PE-TNF (clone MAb11, BioLegend), AF488-ISG15 (clone 851701, R&D Systems), and AF647-IL1B (clone JK1B-1, BioLegend) with a 1:100 dilution. Caspase-1 activity in live cells was assessed using the FAM-FLICA Caspase-1 Assay Kit (Immunochemistry Technologies), following the manufacturer's protocol. Flow cytometry data were acquired on Cytoflex LX (Beckman Coulter) and analyzed using FlowJo v10.1.

Ligand selection
Immune ligands were obtained from InvivoGen and resuspended to stock solutions as specified by the manufacturer. To determine a set of prestimulation conditions for the StimDrop experiment, we first tested 24 different immune ligands at four concentrations (10-fold

dilutions) covering a diverse set of innate immune receptors. We measured viability, cell counts, expression of CD169 and CD86, and bulk RNA-seq profiles after 16 hours of incubation with each condition. We selected the highest concentrations where the monocytes have >85% viability and >40,000 counts and have a significant change in CD86 or CD169 or have more than 10 differentially expressed genes when compared with the unstimulated control. For the StimDrop experiment, three concentrations (either 10-fold or 4-fold dilutions) were selected for each ligand. The conditions tested and used for the StimDrop experiment are detailed in table S1.

Custom hashtag antibody conjugation
Oligonucleotides were conjugated to CD45 antibodies (clone HI30, BioLegend) using the Thunder-Link PLUS Antibody Conjugation Kit (Novus Biologicals) with minor modifications. Amine-modified oligos were obtained from Integrated DNA Technologies with the following sequence: /5AmMC6/GTGACTGGAGTTCA-GACGTGTGCTCTTCCGATCT-[15 bp barcode]-B[A20]A*A*A. Oligos were resuspended at 200 μM with Wash Buffer from the conjugation kit. Each oligo solution was added 1:1 with an Oligo Activation Reagent resuspended in Wash Buffer and incubated at room temperature for 30 min. The Antibody Activation Reagent was resuspended directly in 1 mg/ml of the anti-CD45 antibody solution. Both the activated oligos and antibodies were desalted using Zeba 7K MWCO columns (Thermo Fisher Scientific) and eluted in Wash Buffer. Activated oligos and antibodies were conjugated by incubating the solutions 1:1 for 1 hour at room temperature. The products were kept at 4°C and used within 1 month.

Bulk RNA-seq and data analysis
Bulk RNA-seq was performed using Smart-Seq2 (56) with minor modifications, as described previously (9), using 1000 to 5000 cells as input. All RNA-seq libraries were sequenced with 38 × 38 paired-end reads using NextSeq (Illumina). RNA-seq libraries were sequenced to a depth of >2 million reads per sample. STAR was used to align sequencing reads to the UCSC hg19 transcriptome, and RSEM was used to generate an expression matrix for all samples. Both raw count and transcripts per million data were analyzed using edgeR and custom Python scripts. Gene set enrichment analysis was performed using enrichR (57).

scRNA-seq and data analysis
scRNA-seq was performed as previously described (8, 9). Cells were loaded on the Chromium platform using the 3′ v2 profiling chemistry (10X Genomics). For StimDrop experiments, gene expression libraries were enriched for immune transcripts with the Target Hybridization Kit and the Human Immunology Gene Panel (10X Genomics). Gene expression and hashtag libraries were sequenced to a depth of ~10,000 and ~2000 reads per cell, respectively, on NextSeq 550 (Illumina). The data were aligned to the GRCh38 reference genome using cellranger v3.1 (10X Genomics). Single-cell data analysis was performed using scanpy (58) with the same preprocessing and filtering parameters described in a previous publication (9). Hashtag assignment and doublet removal were performed using demuxEM (59) and compared with genotype-based classifications from souporcell (60), both using default parameters.

cNMF analysis was performed as detailed in a previous publication (25). Briefly, highly variable genes from the primary StimDrop

gene expression data were first selected to filter the gene expression matrix. NMF was then performed with k = 5 to 25 (10 iterations for each k). The number of modules (k) for downstream analysis was selected on the basis of biological interpretability of the modules and stability of the cNMF solution. To ensure that no modules from technical artifacts were analyzed, only gene programs with mean usage > 5 across cells were included for further analysis. To obtain a score for the inflammatory activation gene module in the corresponding bulk RNA-seq experiment, the average expression of top 20 genes from the modules was calculated and subtracted by the average expression of a randomly sampled set of 150 reference genes (61).

ATAC-seq and data analysis

Assay for transposase-accessible chromain with sequencing (ATAC-seq) was performed on 50,000 cells as described in a published protocol (62). Libraries were sequenced on NextSeq (Illumina) with 38 × 38 paired-end reads and at least 10 million reads per sample. Sequencing data were aligned using the ENCODE Project ATAC-seq pipeline (https://encodeproject.org/pages/pipelines/) and further analyzed using custom scripts. To generate a peak count matrix, we first identified a consensus peak set using the multiinter function and analyzed the number of counts for each sample using the function coverageBed from bedtools v2. Transcription factor activity was quantified using motif-displacement scores (63, 64). Differential peak analysis was performed using edgeR, using the peak count matrix as input. The nearest genes for each were analyzed using the annotatePeaks function in HOMER v4.1 (65).

Supplementary Materials

This PDF file includes:
Figs. S1 to S10
Legend for table S1
Legends for data files S1 and S2

Other Supplementary Material for this manuscript includes the following:
Table S1
Data files S1 and S2

View/request a protocol for this paper from *Bio-protocol*.

REFERENCES AND NOTES

1. A. Haque, J. Engel, S. A. Teichmann, T. Lönnberg, A practical guide to single-cell RNA-sequencing for biomedical research and clinical applications. *Genome Med.* **9**, 75 (2017).
2. C. Domínguez Conde, C. Xu, L. B. Jarvis, D. B. Rainbow, S. B. Wells, T. Gomes, S. K. Howlett, O. Suchanek, K. Polanski, H. W. King, L. Mamanova, N. Huang, P. A. Szabo, L. Richardson, L. Bolt, E. S. Fasouli, K. T. Mahbubani, M. Prete, L. Tuck, N. Richoz, Z. K. Tuong, L. Campos, H. S. Mousa, E. J. Needham, S. Pritchard, T. Li, R. Elmentaite, J. Park, E. Rahmani, D. Chen, D. K. Menon, O. A. Bayraktar, L. K. James, K. B. Meyer, N. Yosef, M. R. Clatworthy, P. A. Sims, D. L. Farber, K. Saeb-Parsy, J. L. Jones, S. A. Teichmann, Cross-tissue immune cell analysis reveals tissue-specific features in humans. *Science* **376**, eabl5197 (2022).
3. Tabula Sapiens Consortium, R. C. Jones, J. Karkanias, M. A. Krasnow, A. O. Pisco, S. R. Quake, J. Salzman, N. Yosef, B. Bulthaup, P. Brown, W. Harper, M. Hemenez, R. Ponnusamy, A. Salehi, B. A. Sanagavarapu, E. Spallino, K. A. Aaron, W. Concepcion, J. M. Gardner, B. Kelly, N. Neidlinger, Z. Wang, S. Crasta, S. Kolluru, M. Morri, A. O. Pisco, S. Y. Tan, K. J. Travaglini, C. Xu, M. Alcántara-Hernández, N. Almanzar, J. Antony, B. Beyersdorf, D. Burhan, K. Calcuttawala, M. M. Carter, C. K. F. Chan, C. A. Chang, S. Chang, A. Colville, S. Crasta, R. N. Culver, I. Cvijović, G. D'Amato, C. Ezran, F. X. Galdos, A. Gillich, W. R. Goodyer, Y. Hang, A. Hayashi, S. Houshdaran, X. Huang, J. C. Irwin, S. Jang, J. V. Juanico, A. M. Kershner, S. Kim, B. Kiss, S. Kolluru, W. Kong, M. E. Kumar, A. H. Kuo, R. Leylek, B. Li, G. B. Loeb, W.-J. Lu, S. Mantri, M. Markovic, P. L. McAlpine, A. de Morree, M. Morri, K. Mrouj, S. Mukherjee, T. Muser, P. Neuhöfer, T. D. Nguyen, K. Perez, R. Phansalkar, A. O. Pisco, N. Puluca, Z. Qi, P. Rao, H. Raquer-McKay, N. Schaum, B. Scott, B. Seddighzadeh, J. Segal, S. Sen, S. Sikandar, S. P. Spencer, L. C. Steffes, V. R. Subramaniam, A. Swarup, M. Swift, K. J. Travaglini, W. Van Treuren, E. Trimm, S. Veizades, S. Vijayakumar, K. C. Vo, S. K. Vorperian, W. Wang, H. N. W. Weinstein, J. Winkler, T. T. H. Wu, J. Xie, A. R. Yung, Y. Zhang, A. M. Detweiler, H. Mekonen, N. F. Neff, R. V. Sit, M. Tan, J. Yan, G. R. Bean, V. Charu, E. Forgó, B. A. Martin, M. G. Ozawa, O. Silva, S. Y. Tan, A. Toland, V. N. P. Vemuri, S. Afik, K. Awayan, O. B. Botvinnik, A. Byrne, M. Chen, R. Dehghannasiri, A. M. Detweiler, A. Gayoso, A. A. Granados, Q. Li, G. Mahmoudabadi, A. McGeever, A. de Morree, J. E. Olivieri, M. Park, A. O. Pisco, N. Ravikumar, J. Salzman, G. Stanley, M. Swift, M. Tan, W. Tan, A. J. Tarashansky, R. Vanheusden, S. K. Vorperian, P. Wang, S. Wang, G. Xing, C. Xu, N. Yosef, M. Alcántara-Hernández, J. Antony, C. K. F. Chan, C. A. Chang, A. Colville, S. Crasta, R. Culver, L. Dethlefsen, C. Ezran, A. Gillich, Y. Hang, P.-Y. Ho, J. C. Irwin, S. Jang, A. M. Kershner, W. Kong, M. E. Kumar, A. H. Kuo, R. Leylek, S. Liu, G. B. Loeb, W.-J. Lu, J. S. Maltzman, R. J. Metzger, A. de Morree, P. Neuhöfer, K. Perez, R. Phansalkar, Z. Qi, P. Rao, H. Raquer-McKay, K. Sasagawa, B. Scott, R. Sinha, H. Song, S. P. Spencer, A. Swarup, M. Swift, K. J. Travaglini, E. Trimm, S. Veizades, S. Vijayakumar, B. Wang, W. Wang, J. Winkler, J. Xie, A. R. Yung, S. E. Artandi, P. A. Beachy, M. F. Clarke, L. C. Giudice, F. W. Huang, K. C. Huang, J. Idoyaga, S. K. Kim, M. Krasnow, C. S. Kuo, P. Nguyen, S. R. Quake, T. A. Rando, K. Red-Horse, J. Reiter, D. A. Relman, J. L. Sonnenburg, B. Wang, A. Wu, S. M. Wu, T. Wyss-Coray, The Tabula Sapiens: A multiple-organ, single-cell transcriptomic atlas of humans. *Science* **376**, eabl4896 (2022).
4. G. Eraslan, E. Drokhlyansky, S. Anand, E. Fiskin, A. Subramanian, M. Slyper, J. Wang, N. Van Wittenberghe, J. M. Rouhana, J. Waldman, O. Ashenberg, M. Lek, D. Dionne, T. S. Win, M. S. Cuoco, O. Kuksenko, A. M. Tsankov, P. A. Branton, J. L. Marshall, A. Greka, G. Getz, A. V. Segrè, F. Aguet, O. Rozenblatt-Rosen, K. G. Ardlie, A. Regev, Single-nucleus cross-tissue molecular reference maps toward understanding disease gene function. *Science* **376**, eabl4290 (2022).
5. S. Pandey, A. Gruenbaum, T. Kanashova, P. Mertins, P. Cluzel, N. Chevrier, Pairwise stimulations of pathogen-sensing pathways predict immune responses to multi-adjuvant combinations. *Cell Syst.* **11**, 495–508.e10 (2020).
6. B. Lin, B. Dutta, I. D. C. Fraser, Systematic investigation of multi-TLR sensing identifies regulators of sustained gene activation in macrophages. *Cell Syst.* **5**, 25–37.e3 (2017).
7. E. Platanitis, T. Decker, Regulatory networks involving STATs, IRFs, and NFκB in Inflammation. *Front. Immunol.* **9**, 2542 (2018).
8. M. Reyes, M. R. Filbin, R. P. Bhattacharyya, K. Billman, T. Eisenhaure, D. T. Hung, B. D. Levy, R. M. Baron, P. C. Blainey, M. B. Goldberg, N. Hacohen, An immune-cell signature of bacterial sepsis. *Nat. Med.* **26**, 333–340 (2020).
9. M. Reyes, M. R. Filbin, R. P. Bhattacharyya, A. Sonny, A. Mehta, K. Billman, K. R. Kays, M. Pinilla-Vera, M. E. Benson, L. A. Cosimi, D. T. Hung, B. D. Levy, A.-C. Villani, M. Sade-Feldman, R. M. Baron, M. B. Goldberg, P. C. Blainey, N. Hacohen, Plasma from patients with bacterial sepsis or severe COVID-19 induces suppressive myeloid cell production from hematopoietic progenitors in vitro. *Sci. Transl. Med.* **13**, eabe9599 (2021).
10. K. Bassler, J. Schulte-Schrepping, S. Warnat-Herresthal, A. C. Aschenbrenner, J. L. Schultze, The myeloid cell compartment-cell by cell. *Annu. Rev. Immunol.* **37**, 269–293 (2019).
11. H. Zheng, A. M. Rao, D. Dermadi, J. Toh, L. Murphy Jones, M. Donato, Y. Liu, Y. Su, C. L. Dai, S. A. Kornilov, M. Karagiannis, T. Marantos, Y. Hasin-Brumshtein, Y. D. He, E. J. Giamarellos-Bourboulis, J. R. Heath, P. Khatri, Multi-cohort analysis of host immune response identifies conserved protective and detrimental modules associated with severity across viruses. *Immunity* **54**, 753–768.e5 (2021).
12. J. Schulte-Schrepping, N. Reusch, D. Paclik, K. Baßler, S. Schlickeiser, B. Zhang, B. Krämer, T. Krammer, S. Brumhard, L. Bonaguro, E. De Domenico, D. Wendisch, M. Grasshoff, T. S. Kapellos, M. Beckstette, T. Pecht, A. Saglam, O. Dietrich, H. E. Mei, A. R. Schulz, C. Conrad, D. Kunkel, E. Vafadarnejad, C.-J. Xu, A. Horne, M. Herbert, A. Drews, C. Thibeault, M. Pfeiffer, S. Hippenstiel, A. Hocke, H. Müller-Redetzky, K.-M. Heim, F. Machleidt, A. Uhrig, L. Bosquillon de Jarcy, L. Jürgens, M. Stegemann, C. R. Glösenkamp, H.-D. Volk, C. Goffinet, E. Landthaler, P. Wyler, M. Georg, M. Schneider, C. Dang-Heine, N. Neuwinger, K. Kappert, R. Tauber, V. Corman, J. Raabe, K. M. Kaiser, M. T. Vinh, G. Rieke, C. Meisel, T. Ulas, M. Becker, R. Geffers, M. Witzenrath, C. Drosten, N. Suttorp, C. von Kalle, F. Kurth, K. Händler, J. L. Schultze, A. C. Aschenbrenner, Y. Li, J. Nattermann, B. Sawitzki, A.-E. Saliba, L. E. Sander; Deutsche COVID-19 OMICS Initiative (DeCOI), Severe COVID-19 is marked by a dysregulated myeloid cell compartment. *Cell* **182**, 1419–1440.e23 (2020).
13. Y. Okabe, R. Medzhitov, Tissue biology perspective on macrophages. *Nat. Immunol.* **17**, 9–17 (2016).
14. S. L. Foster, D. C. Hargreaves, R. Medzhitov, Gene-specific control of inflammation by TLR-induced chromatin modifications. *Nature* **447**, 972–978 (2007).
15. J. Quintin, S. Saeed, J. H. A. Martens, E. J. Giamarellos-Bourboulis, D. C. Ifrim, C. Logie, L. Jacobs, T. Jansen, B.-J. Kullberg, C. Wijmenga, L. A. B. Joosten, R. J. Xavier, J. W. M. van der Meer, H. G. Stunnenberg, M. G. Netea, *Candida albicans* infection affords protection

against reinfection via functional reprogramming of monocytes. *Cell Host Microbe* **12**, 223–232 (2012).

16. E. Kaufmann, J. Sanz, J. L. Dunn, N. Khan, L. E. Mendonça, A. Pacis, F. Tzelepis, E. Pernet, A. Dumaine, J.-C. Grenier, F. Mailhot-Léonard, E. Ahmed, J. Belle, R. Besla, B. Mazer, I. L. King, A. Nijnik, C. S. Robbins, L. B. Barreiro, M. Divangahi, BCG educates hematopoietic stem cells to generate protective innate immunity against tuberculosis. *Cell* **172**, 176–190.e19 (2018).

17. J. A. McCullers, The co-pathogenesis of influenza viruses with bacteria in the lung. *Nat. Rev. Microbiol.* **12**, 252–262 (2014).

18. M. Merad, J. C. Martin, Pathological inflammation in patients with COVID-19: A key role for monocytes and macrophages. *Nat. Rev. Immunol.* **20**, 355–362 (2020).

19. A. Ablasser, Z. J. Chen, cGAS in action: Expanding roles in immunity and inflammation. *Science* **363**, eaat8657 (2019).

20. K. T. Chow, M. Gale Jr., Y.-M. Loo, RIG-I and other RNA sensors in antiviral immunity. *Annu. Rev. Immunol.* **36**, 667–694 (2018).

21. G. D. Brown, J. A. Willment, L. Whitehead, C-type lectins in immunity and homeostasis. *Nat. Rev. Immunol.* **18**, 374–389 (2018).

22. T. Kawai, S. Akira, The role of pattern-recognition receptors in innate immunity: Update on Toll-like receptors. *Nat. Immunol.* **11**, 373–384 (2010).

23. A. Kulesa, J. Kehe, J. E. Hurtado, P. Tawde, P. C. Blainey, Combinatorial drug discovery in nanoliter droplets. *Proc. Natl. Acad. Sci. U.S.A.* **115**, 6685–6690 (2018).

24. M. Stoeckius, S. Zheng, B. Houck-Loomis, S. Hao, B. Z. Yeung, W. M. Mauck III, P. Smibert, R. Satija, Cell hashing with barcoded antibodies enables multiplexing and doublet detection for single cell genomics. *Genome Biol.* **19**, 224 (2018).

25. D. Kotliar, A. Veres, M. A. Nagy, S. Tabrizi, E. Hodis, D. A. Melton, P. C. Sabeti, Identifying gene expression programs of cell-type identity and cellular activity with single-cell RNA-Seq. *eLife* **8**, ee43803 (2019).

26. V. A. K. Rathinam, Z. Jiang, S. N. Waggoner, S. Sharma, L. E. Cole, L. Waggoner, S. K. Vanaja, B. G. Monks, S. Ganesan, E. Latz, V. Hornung, S. N. Vogel, E. Szomolanyi-Tsuda, K. A. Fitzgerald, The AIM2 inflammasome is essential for host defense against cytosolic bacteria and DNA viruses. *Nat. Immunol.* **11**, 395–402 (2010).

27. M. Relloso, A. Puig-Kröger, O. M. Pello, J. L. Rodríguez-Fernández, G. de la Rosa, N. Longo, J. Navarro, M. A. Muñoz-Fernández, P. Sánchez-Mateos, A. L. Corbí, DC-SIGN (CD209) expression is IL-4 dependent and is negatively regulated by IFN, TGF-β, and anti-inflammatory agents. *J. Immunol.* **168**, 2634–2643 (2002).

28. M. Gentili, J. Kowal, M. Tkach, T. Satoh, X. Lahaye, C. Conrad, M. Boyron, B. Lombard, S. Durand, G. Kroemer, D. Loew, M. Dalod, C. Théry, N. Manel, Transmission of innate immune signaling by packaging of cGAMP in viral particles. *Science* **349**, 1232–1236 (2015).

29. A.-C. Villani, R. Satija, G. Reynolds, S. Sarkizova, K. Shekhar, J. Fletcher, M. Griesbeck, A. Butler, S. Zheng, S. Lazo, L. Jardine, D. Dixon, E. Stephenson, E. Nilsson, I. Grundberg, D. McDonald, A. Filby, W. Li, P. L. De Jager, O. Rozenblatt-Rosen, A. A. Lane, M. Haniffa, A. Regev, N. Hacohen, Single-cell RNA-seq reveals new types of human blood dendritic cells, monocytes, and progenitors. *Science* **356**, eaah4573 (2017).

30. X. Chen, X. Liu, Y. Zhang, W. Huai, Q. Zhou, S. Xu, X. Chen, N. Li, X. Cao, Methyltransferase Dot1l preferentially promotes innate IL-6 and IFN-β production by mediating H3K79me2/3 methylation in macrophages. *Cell. Mol. Immunol.* **17**, 76–84 (2020).

31. L. Kruidenier, C.-W. Chung, Z. Cheng, J. Liddle, K. Che, G. Joberty, M. Bantscheff, C. Bountra, A. Bridges, H. Diallo, D. Eberhard, S. Hutchinson, E. Jones, R. Katso, M. Leveridge, P. K. Mander, J. Mosley, C. Ramirez-Molina, P. Rowland, C. J. Schofield, R. J. Sheppard, J. E. Smith, C. Swales, R. Tanner, P. Thomas, A. Tumber, G. Drewes, U. Oppermann, D. J. Patel, K. Lee, D. M. Wilson, A selective jumonji H3K27 demethylase inhibitor modulates the proinflammatory macrophage response. *Nature* **488**, 404–408 (2012).

32. T. Satoh, O. Takeuchi, A. Vandenbon, K. Yasuda, Y. Tanaka, Y. Kumagai, T. Miyake, K. Matsushita, T. Okazaki, T. Saitoh, K. Honma, T. Matsuyama, K. Yui, T. Tsujimura, D. M. Standley, K. Nakanishi, K. Nakai, S. Akira, The Jmjd3-*Irf4* axis regulates M2 macrophage polarization and host responses against helminth infection. *Nat. Immunol.* **11**, 936–944 (2010).

33. P. Bost, A. Giladi, Y. Liu, Y. Bendjelal, G. Xu, E. David, R. Blecher-Gonen, M. Cohen, C. Medaglia, H. Li, A. Deczkowska, S. Zhang, B. Schwikowski, Z. Zhang, I. Amit, Host-viral infection maps reveal signatures of severe COVID-19 patients. *Cell* **181**, 1475–1488.e12 (2020).

34. D. K. Singh, E. Aladyeva, S. Das, B. Singh, E. Esaulova, A. Swain, M. Ahmed, J. Cole, C. Moodley, S. Mehra, L. S. Schlesinger, M. N. Artyomov, S. A. Khader, D. Kaushal, Myeloid cell interferon responses correlate with clearance of SARS-CoV-2. *Nat. Commun.* **13**, 679 (2022).

35. J.-L. Casanova, L. Abel, Mechanisms of viral inflammation and disease in humans. *Science* **374**, 1080–1086 (2021).

36. T. Shu, W. Ning, D. Wu, J. Xu, Q. Han, M. Huang, X. Zou, Q. Yang, Y. Yuan, Y. Bie, S. Pan, J. Mu, Y. Han, X. Yang, H. Zhou, R. Li, Y. Ren, X. Chen, S. Yao, Y. Qiu, D.-Y. Zhang, Y. Xue, Y. Shang, X. Zhou, Plasma proteomics identify biomarkers and pathogenesis of COVID-19. *Immunity* **53**, 1108–1122.e5 (2020).

37. B. Shen, X. Yi, Y. Sun, X. Bi, J. Du, C. Zhang, S. Quan, F. Zhang, R. Sun, L. Qian, W. Ge, W. Liu, S. Liang, H. Chen, Y. Zhang, J. Li, J. Xu, Z. He, B. Chen, J. Wang, H. Yan, Y. Zheng, D. Wang, J. Zhu, Z. Kong, Z. Kang, X. Liang, X. Ding, G. Ruan, N. Xiang, X. Cai, H. Gao, L. Li, S. Li, Q. Xiao, T. Lu, Y. Zhu, H. Liu, H. Chen, T. Guo, Proteomic and metabolomic characterization of COVID-19 patient sera. *Cell* **182**, 59–72.e15 (2020).

38. M. R. Filbin, A. Mehta, A. M. Schneider, K. R. Kays, J. R. Guess, M. Gentili, B. G. Fenyves, N. C. Charland, A. L. K. Gonye, I. Gushterova, H. K. Khanna, T. J. LaSalle, K. M. Lavin-Parsons, B. M. Lilley, C. L. Lodenstein, K. Manakongtreecheep, J. D. Margolin, B. N. McKaig, M. Rojas-Lopez, B. C. Russo, N. Sharma, J. Tantivit, M. F. Thomas, R. E. Gerszten, G. S. Heimberg, P. J. Hoover, D. J. Lieb, B. Lin, D. Ngo, K. Pelka, M. Reyes, C. S. Smillie, A. Waghray, T. E. Wood, A. S. Zajac, L. L. Jennings, I. Grundberg, R. P. Bhattacharyya, B. A. Parry, A.-C. Villani, M. Sade-Feldman, N. Hacohen, M. B. Goldberg, Longitudinal proteomic analysis of severe COVID-19 reveals survival-associated signatures, tissue-specific cell death, and cell-cell interactions. *Cell Rep. Med.* **2**, 100287 (2021).

39. R. A. Grant, L. Morales-Nebreda, N. S. Markov, S. Swaminathan, M. Querrey, E. R. Guzman, D. A. Abbott, H. K. Donnelly, A. Donayre, I. A. Goldberg, Z. M. Klug, N. Borkowski, Z. Lu, H. Kihshen, Y. Politanska, L. Sichizya, M. Kang, A. Shilatifard, C. Qi, J. W. Lomasney, A. C. Argento, J. M. Kruser, E. S. Malsin, C. O. Pickens, S. B. Smith, J. M. Walter, A. E. Pawlowski, D. Schneider, P. Nannapaneni, H. Abdala-Valencia, A. Bharat, C. J. Gottardi, G. R. S. Budinger, A. V. Misharin, B. D. Singer, R. G. Wunderink; NU SCRIPT Study Investigators, Circuits between infected macrophages and T cells in SARS-CoV-2 pneumonia. *Nature* **590**, 635–641 (2021).

40. M. Liao, Y. Liu, J. Yuan, Y. Wen, G. Xu, J. Zhao, L. Cheng, J. Li, X. Wang, F. Wang, L. Liu, I. Amit, S. Zhang, Z. Zhang, Single-cell landscape of bronchoalveolar immune cells in patients with COVID-19. *Nat. Med.* **26**, 842–844 (2020).

41. P. A. Szabo, P. Dogra, J. I. Gray, S. B. Wells, T. J. Connors, S. P. Weisberg, I. Krupska, R. Matsumoto, M. M. L. Poon, E. Idzikowski, S. E. Morris, C. Pasin, A. J. Yates, A. Ku, M. Chait, J. Davis-Porada, X. V. Guo, J. Zhou, M. Steinle, S. Mackay, A. Saqi, M. R. Baldwin, P. A. Sims, D. L. Farber, Longitudinal profiling of respiratory and systemic immune responses reveals myeloid cell-driven lung inflammation in severe COVID-19. *Immunity* **54**, 797–814.e6 (2021).

42. S. Trump, S. Lukassen, M. S. Anker, R. L. Chua, J. Liebig, L. Thürmann, V. M. Corman, M. Binder, J. Loske, C. Klasa, T. Krieger, B. P. Hennig, M. Messingschlager, F. Pott, J. Kazmierski, S. Twardziok, J. P. Albrecht, J. Eils, S. Hadzibegovic, A. Lena, B. Heidecker, T. Bürgel, J. Steinfeldt, C. Goffinet, F. Kurth, M. Witzenrath, M. T. Völker, S. D. Müller, U. G. Liebert, N. Ishaque, L. Kaderali, L.-E. Sander, C. Drosten, S. Laudi, R. Eils, C. Conrad, U. Landmesser, I. Lehmann, Hypertension delays viral clearance and exacerbates airway hyperinflammation in patients with COVID-19. *Nat. Biotechnol.* **39**, 705–716 (2021).

43. P. S. Arunachalam, F. Wimmers, C. K. P. Mok, R. A. P. M. Perera, M. Scott, T. Hagan, N. Sigal, Y. Feng, L. Bristow, O. Tak-Yin Tsang, D. Wagh, J. Coller, K. L. Pellegrini, D. Kazmin, G. Alaaeddine, W. S. Leung, J. M. C. Chan, T. S. H. Chik, C. Y. C. Choi, C. Huerta, M. Paine McCullough, H. Lv, E. Anderson, S. Edupuganti, A. A. Upadhyay, S. E. Bosinger, H. T. Maecker, P. Khatri, N. Rouphael, M. Peiris, B. Pulendran, Systems biological assessment of immunity to mild versus severe COVID-19 infection in humans. *Science* **369**, 1210–1220 (2020).

44. M. Venzon, L. Bernard-Raichon, J. Klein, J. E. Axelrad, C. Zhang, G. A. Hussey, A. P. Sullivan, A. Casanovas-Massana, M. G. Noval, A. M. Valero-Jimenez, J. Gago, G. Putzel, A. Pironti, E. Wilder, Yale IMPACT Research Team, L. E. Thorpe, D. R. Littman, M. Dittmann, K. A. Stapleford, B. Shopsin, V. J. Torres, A. I. Ko, A. Iwasaki, K. Cadwell, J. Schluter, Gut microbiome dysbiosis during COVID-19 is associated with increased risk for bacteremia and microbial translocation. bioRxiv 2021.07.15.452246 [**Preprint**]. 2 March 2022. https://doi.org/10.1101/2021.07.15.452246.

45. N. Shafran, I. Shafran, H. Ben-Zvi, S. Sofer, L. Sheena, I. Krause, A. Shlomai, E. Goldberg, E. H. Sklan, Secondary bacterial infection in COVID-19 patients is a stronger predictor for death compared to influenza patients. *Sci. Rep.* **11**, 12703 (2021).

46. E. Wauters, P. Van Mol, A. D. Garg, S. Jansen, Y. Van Herck, L. Vanderbeke, A. Bassez, B. Boeckx, B. Malengier-Devlies, A. Timmerman, T. Van Brussel, T. Van Buyten, R. Schepers, E. Heylen, D. Dauwe, C. Dooms, J. Gunst, G. Hermans, P. Meersseman, D. Testelmans, J. Yserbyt, S. Tejpar, W. De Wever, P. Matthys; CONTAGIOUS collaborators, J. Neyts, J. Wauters, J. Qian, D. Lambrechts, Discriminating mild from critical COVID-19 by innate and adaptive immune single-cell profiling of bronchoalveolar lavages. *Cell Res.* **31**, 272–290 (2021).

47. A. Wang, S. D. Pope, J. S. Weinstein, S. Yu, C. Zhang, C. J. Booth, R. Medzhitov, Specific sequences of infectious challenge lead to secondary hemophagocytic lymphohistiocytosis-like disease in mice. *Proc. Natl. Acad. Sci. U.S.A.* **116**, 2200–2209 (2019).

48. A. M. Jamieson, L. Pasman, S. Yu, P. Gamradt, R. J. Homer, T. Decker, R. Medzhitov, Role of tissue protection in lethal respiratory viral-bacterial coinfection. *Science* **340**, 1230–1234 (2013).

49. L. Bernard-Raichon, M. Venzon, J. Klein, J. E. Axelrad, C. Zhang, A. P. Sullivan, G. A. Hussey, A. Casanovas-Massana, M. G. Noval, A. M. Valero-Jimenez, J. Gago, G. Putzel, A. Pironti, E. Wilder; Yale IMPACT Research Team, L. E. Thorpe, D. R. Littman, M. Dittmann, K. A. Stapleford, B. Shopsin, V. J. Torres, A. I. Ko, A. Iwasaki, K. Cadwell, J. Schluter, Gut microbiome dysbiosis in antibiotic-treated COVID-19 patients is associated with microbial translocation and bacteremia. *Nat. Commun.* **13**, 5926 (2022).

50. J. Kehe, A. Kulesa, A. Ortiz, C. M. Ackerman, S. G. Thakku, D. Sellers, S. Kuehn, J. Gore, J. Friedman, P. C. Blainey, Massively parallel screening of synthetic microbial communities. *Proc. Natl. Acad. Sci. U.S.A.* **116**, 12804–12809 (2019).

51. S. Varma, J. Voldman, Caring for cells in microsystems: Principles and practices of cell-safe device design and operation. *Lab Chip* **18**, 3333–3352 (2018).

52. C. S. McGinnis, D. M. Patterson, J. Winkler, D. N. Conrad, M. Y. Hein, V. Srivastava, J. L. Hu, L. M. Murrow, J. S. Weissman, Z. Werb, E. D. Chow, Z. J. Gartner, MULTI-seq: Sample multiplexing for single-cell RNA sequencing using lipid-tagged indices. *Nat. Methods* **16**, 619–626 (2019).

53. C. Guo, W. Kong, K. Kamimoto, G. C. Rivera-Gonzalez, X. Yang, Y. Kirita, S. A. Morris, CellTag Indexing: Genetic barcode-based sample multiplexing for single-cell genomics. *Genome Biol.* **20**, 90 (2019).

54. D. Shin, W. Lee, J. H. Lee, D. Bang, Multiplexed single-cell RNA-seq via transient barcoding for simultaneous expression profiling of various drug perturbations. *Sci. Adv.* **5**, eaav2249 (2019).

55. S. R. Srivatsan, J. L. McFaline-Figueroa, V. Ramani, L. Saunders, J. Cao, J. Packer, H. A. Pliner, D. L. Jackson, R. M. Daza, L. Christiansen, F. Zhang, F. Steemers, J. Shendure, C. Trapnell, Massively multiplex chemical transcriptomics at single-cell resolution. *Science* **367**, 45–51 (2020).

56. S. Picelli, O. R. Faridani, A. K. Björklund, G. Winberg, S. Sagasser, R. Sandberg, Full-length RNA-seq from single cells using Smart-seq2. *Nat. Protoc.* **9**, 171–181 (2014).

57. Z. Xie, A. Bailey, M. V. Kuleshov, D. J. B. Clarke, J. E. Evangelista, S. L. Jenkins, A. Lachmann, M. L. Wojciechowicz, E. Kropiwnicki, K. M. Jagodnik, M. Jeon, A. Ma'ayan, Gene set knowledge discovery with Enrichr. *Curr. Protoc.* **1**, e90 (2021).

58. F. A. Wolf, P. Angerer, F. J. Theis, SCANPY: Large-scale single-cell gene expression data analysis. *Genome Biol.* **19**, 15 (2018).

59. J. T. Gaublomme, B. Li, C. McCabe, A. Knecht, Y. Yang, E. Drokhlyansky, N. Van Wittenberghe, J. Waldman, D. Dionne, L. Nguyen, P. L. De Jager, B. Yeung, X. Zhao, N. Habib, O. Rozenblatt-Rosen, A. Regev, Nuclei multiplexing with barcoded antibodies for single-nucleus genomics. *Nat. Commun.* **10**, 2907 (2019).

60. H. Heaton, A. M. Talman, A. Knights, M. Imaz, D. J. Gaffney, R. Durbin, M. Hemberg, M. K. N. Lawniczak, Souporcell: Robust clustering of single-cell RNA-seq data by genotype without reference genotypes. *Nat. Methods* **17**, 615–620 (2020).

61. R. Satija, J. A. Farrell, D. Gennert, A. F. Schier, A. Regev, Spatial reconstruction of single-cell gene expression data. *Nat. Biotechnol.* **33**, 495–502 (2015).

62. M. R. Corces, A. E. Trevino, E. G. Hamilton, P. G. Greenside, N. A. Sinnott-Armstrong, S. Vesuna, A. T. Satpathy, A. J. Rubin, K. S. Montine, B. Wu, A. Kathiria, S. W. Cho, M. R. Mumbach, A. C. Carter, M. Kasowski, L. A. Orloff, V. I. Risca, A. Kundaje, P. A. Khavari, T. J. Montine, W. J. Greenleaf, H. Y. Chang, An improved ATAC-seq protocol reduces background and enables interrogation of frozen tissues. *Nat. Methods* **14**, 959–962 (2017).

63. J. G. Azofeifa, M. A. Allen, J. R. Hendrix, T. Read, J. D. Rubin, R. D. Dowell, Enhancer RNA profiling predicts transcription factor activity. *Genome Res.* **28**, 334–344 (2018).

64. I. J. Tripodi, M. A. Allen, R. D. Dowell, Detecting differential transcription factor activity from ATAC-seq data. *Molecules* **23**, 1136 (2018).

65. S. Heinz, C. Benner, N. Spann, E. Bertolino, Y. C. Lin, P. Laslo, J. X. Cheng, C. Murre, H. Singh, C. K. Glass, Simple combinations of lineage-determining transcription factors prime cis-regulatory elements required for macrophage and B cell identities. *Mol. Cell* **38**, 576–589 (2010).